

Article

Stable Patterns in the Lugiato–Lefever Equation with a Confined Vortex Pump

Shatrughna Kumar ¹, Wesley B. Cardoso ²  and Boris A. Malomed ^{1,3,*} 

¹ Department of Physical Electronics, School of Electrical Engineering, Faculty of Engineering, and Center for Light-Matter Interaction, Tel Aviv University, Tel Aviv 69978, Israel; shatrughna@mail.tau.ac.il

² Instituto de Física, Universidade Federal de Goiás, Goiânia 74690-900, Goiás, Brazil; wesleybcardoso@ufg.br

³ Instituto de Alta Investigación, Universidad de Tarapacá, Casilla 7D, Arica 1000000, Chile

* Correspondence: malomed@tauex.tau.ac.il

Abstract: We introduce a model of a passive optical cavity based on a novel variety of the two-dimensional Lugiato–Lefever equation, with a localized pump carrying intrinsic vorticity S , and the cubic or cubic–quintic nonlinearity. Up to $S = 5$, stable confined vortex ring states (vortex pixels) are produced by means of a variational approximation and in a numerical form. Surprisingly, vast stability areas of the vortex states are found, for both the self-focusing and defocusing signs of the nonlinearity, in the plane of the pump and loss parameters. When the vortex rings are unstable, they are destroyed by azimuthal perturbations, which break the axial symmetry. The results suggest new possibilities for mode manipulations in passive nonlinear photonic media by means of appropriately designed pump beams.

Keywords: nonlinear optical cavity; cubic-quintic nonlinearity; localized pump; vortex ring states; vortex pixels

1. Introduction and the Model



Citation: Kumar, S.; Cardoso, W.B.; Malomed, B.A. Stable Patterns in the Lugiato–Lefever Equation with a Confined Vortex Pump. *Symmetry* **2024**, *16*, 470. <https://doi.org/10.3390/sym16040470>

Academic Editor: Mariano Torrisi

Received: 28 February 2024

Revised: 30 March 2024

Accepted: 3 April 2024

Published: 12 April 2024



Copyright: © 2024 by the authors. Licensee MDPI, Basel, Switzerland. This article is an open access article distributed under the terms and conditions of the Creative Commons Attribution (CC BY) license (<https://creativecommons.org/licenses/by/4.0/>).

Optical solitons are a broad class of self-trapped states maintained by the interplay of nonlinearity and dispersion or diffraction in diverse photonic media [1,2]. In addition to that, dissipative optical solitons are supported by the equilibrium of loss and gain or pump, which is concomitant to the nonlinearity–dispersion/diffraction balance [3,4]. Dissipative solitons have been studied in detail, theoretically and experimentally, in active setups, with the loss compensated by local gain (essentially provided by lasing) being modeled by one- and two-dimensional (1D and 2D) equations of the complex Ginzburg–Landau (CGL) type [5,6].

In passive nonlinear optical cavities, the losses are balanced by the pump field supplied by external laser beams, with the appropriate models provided by the Lugiato–Lefever (LL) equations [7]. This setting was also studied in the 1D and 2D forms [8–11]. Widely applied in nonlinear optics, equations of the LL type play a crucial role in understanding fundamental phenomena such as the modulation instability (MI) and pattern formation in dissipative environments [8–24]. The relevance of these models extends to the exploration of complex dynamics of various nonlinear photonic modes, with tremendously important applications being the generation of Kerr solitons and frequency combs in passive cavities [12–24], as well as the generation of terahertz radiation [25]. In addition to rectilinear cavity resonators, circular ones can be used too [26]. In many cases, they operate in the whispering gallery regime [27–32].

In most cases, solutions of the one- and two-dimensional LL equations are looked for under the action of a spatially uniform pump, which approximately corresponds to the usual experimental setup. However, the use of localized (focused) pump beams is possible too, which makes it relevant to consider LL equations with the respective shape of the pump terms. In fact, truly localized optical modes in the cavities can be created

only in this case; otherwise, the uniform pump supports the nonzero background of the optical field. In particular, exact analytical solutions of the LL equations with the 1D pump represented by the delta function and approximate solutions maintained by the 2D pump in the form of a Gaussian were reported in Ref. [33]. In Ref. [26], the LL equation for the ring resonator with localized pump and loss terms produced nonlinear resonances leading to the multistability of nonlinear modes and coexisting solitons that are associated with spectrally distinct frequency combs.

Furthermore, solutions for fully localized robust pixels with zero background were produced by the 2D LL equation, thereby incorporating the spatially uniform pump, self-focusing or defocusing cubic nonlinearity, and a tight confining harmonic oscillator potential [34]. Additionally, this model with a vorticity-carrying pump gives rise to stable vortex pixels. In particular, in the case of the self-defocusing sign of the nonlinear term, the pixels with zero vorticity and ones with vorticity $S = 1$ were predicted analytically by means of the Thomas–Fermi (TF) approximation.

In this work, we introduce the 2D LL equation for a complex amplitude field $u(x, y, t)$ of the light field with cubic or cubic–quintic nonlinearity:

$$\frac{\partial u}{\partial t} = -\alpha u + \frac{i}{2} \nabla^2 u + i\sigma(|u|^2 - \eta^2)u - ig(|u|^4 - \eta^4)u + f(r)e^{iS\theta}, \quad (1)$$

and a confined pump beam represented by factor $f(r)$. Here, i is the imaginary unit, $\alpha > 0$ is the loss parameter, $\sigma = +1$ and -1 correspond, respectively, to the self-focusing and defocusing Kerr (cubic) nonlinearity, $g > 0$ or $g < 0$ represent the self-defocusing or focusing quintic nonlinearity (which often occurs in optical media [35–37] in addition to the cubic term), parameter η defines the cavity mismatch—which is $\sigma\eta^2 - g\eta^4$ (the coefficient multiplying the linear term $\sim -iu$) in terms of the linearized LL equation—and

$$f(r) = f_0 r^S \exp(-r^2/W^2) \quad (2)$$

written in terms of polar coordinates (r, θ) , which corresponds to the confined pump beam with real amplitude f_0 , radial width W , and integer vorticity $S \geq 1$. Vortex beams, shaped by the passage of the usual laser beam through an appropriate phase mask, are available in the experiment [37].

Equation (1) is written in the scaled form. All figures (Figures 1–13) are plotted below in the same notation. In physical units, $r = 1$ and $t = 1$ normally correspond to ~ 50 m and ~ 50 ps, respectively. Then, the typical width $W = 2$, considered below, corresponds to the pump beam with diameter ~ 100 m, which is an experimentally relevant value. Accordingly, the characteristic evolution time in simulations presented below, $t \sim 100$, corresponds to the time ~ 5 ns.

Stationary solutions of Equation (1) are characterized by values of the total power (alias norm):

$$P = \int_{-\infty}^{+\infty} dx \int_{-\infty}^{+\infty} dy |u(x, y)|^2 \equiv 2\pi \int_0^{\infty} |u(r, t)|^2 r dr, \quad (3)$$

and the angular momentum is characterized as

$$M = i \int_{-\infty}^{+\infty} dx \int_{-\infty}^{+\infty} dy u^* (y \partial_x u - x \partial_y u) dx dy \quad (4)$$

(with $*$ standing for the complex conjugate), even if the power and angular momentum are not dynamical invariants of the dissipative Equation (1). In the case of the axisymmetric solutions with vorticity S , i.e., $u(x, y) = u(r)e^{iS\theta}$ [38–40], the expressions for the power and angular momentum are simplified:

$$P = 2\pi \int_0^{\infty} |u(r)|^2 r dr, M = SP. \quad (5)$$

Our objective is to construct *stable* ring-shaped vortex solitons (representing vortex pixels in terms of plausible applications) as localized solutions of Equation (1) with the same S as in the pump term (2). The stability is a challenging problem, as it is well known from the work with models based on the nonlinear Schrödinger and CGL equations that (in the absence of a tight confining potential) vortex ring solitons are normally vulnerable to splitting instability. In the case of a narrow ring shape, the splitting instability may be considered as quasi-one-dimensional MI of the ring against azimuthal perturbations, which break its axial symmetry [2,40]. The azimuthal MI is driven by the self-focusing nonlinearity and inhibited by the self-defocusing.

To produce stationary solutions for the vortex solitons in an approximate analytical form (parallel to the numerical solution), we employ a variational approximation (VA). Our results identify regions of the existence and stability of the vortex solitons with $1 \leq S \leq 4$ in the space of parameters of Equations (1) and (2) (in particular, in the plane of (f_0, α)) for both signs of the cubic nonlinearity, $\sigma = \pm 1$, while the mismatch parameter is fixed to be $\eta = 1$ by the dint of scaling. The stability areas are vast, provided that the loss coefficient α is, roughly speaking, not too small. A majority of the results are produced for the pure cubic model, with $g = 0$, but the effect of the quintic term, with $g \neq 0$, is considered too. Quite surprisingly, a stability area for the vortices with $S \leq 3$ was found even in the case of $\sigma = +1, g < 0$, when both the cubic and quintic terms were self-focusing, which usually implies a strong propensity to the azimuthal instability of the vortex rings [40].

The rest of the paper is structured as follows. The analytical approach, based on the appropriate VA, is presented in Section 2. An asymptotic expression for the tail of the vortex solitons, decaying at $r \rightarrow \infty$, is found too in that section. Systematically produced numerical results for the shape and stability of the vortex solitons are collected (and compared to the VA predictions) in Section 3. The paper is concluded by Section 4.

2. Analytical Considerations

This section summarizes the analytical part of the work and results produced by this part. Two directions of the analytical considerations for the present model are possible: the investigation of the decaying “tails” of the localized stationary states, in the framework of the linearized model, and the detailed development of the VA for the full model, including the nonlinear terms.

2.1. Asymptotic Forms of the Vortex Solitons

Direct consideration of the linearized version of Equations (1) and (2) readily produces an explicit result for the soliton’s tail decaying at $r \rightarrow \infty$:

$$u(r, \theta) \approx (i/2)W^4 r^{S-2} \exp(-r^2/W^2 + iS\theta), \quad (6)$$

with the power of the pre-Gaussian factor, r^{S-2} , which is lower than that in the pump term, r^S . Due to this feature, the asymptotic expression (6) formally predicts a maximum of local power $|u(r)|^2$ at $S > 2$, where

$$r^2 = r_{\max}^2 \equiv \sqrt{(S/2 - 1)}W. \quad (7)$$

A local maximum was indeed observed in numerically found radial profiles of all the vortex solitons. In fact, for these cases Equation (7) predicted values of r_{\max} which were smaller by a factor $\simeq 0.6$ than the actually observed positions of the maxima. The discrepancy is explained by the fact that the asymptotic expression (6) is valid at values of r which are essentially larger than r_{\max} .

In a looser form, one can try to construct an asymptotic approximation for the solution at moderately large r by adopting the *ansatz*, which follows the functional form of the pump term (2), viz.,

$$u(r, \theta) \approx u(r)r^S \exp(-r^2/W^2 + iS\theta), \quad (8)$$

where $u(r)$ is a complex slowly varying function in comparison with those which are explicitly present in the *ansatz* (8). By substituting the *ansatz* in Equation (1) and omitting derivatives of the slowly varying function, one can develop an approach that is akin to the TF approximation applied to the model with the tight trapping potential in Ref. [33]. The result for the linearized version of Equation (1), which implies a small amplitude of the mode pinned to the pump beam, is

$$u(r) = f_0 \left[\alpha - i \left(\frac{2r^2}{W^4} - \frac{2(S+1)}{W^2} - \sigma + g \right) \right]^{-1}, \quad (9)$$

where, as said above, $\eta = 1$ is substituted. In the limit of $r \rightarrow \infty$, Equations (8) and (9) carry over into the asymptotically rigorous expression (6). On the other hand, Equation (9) predicts a maximum of the local power at

$$r^2 = (r_{\max}^2)_{\text{TF}} = (S+1)W^2 + \frac{\sigma-g}{2}W^4, \quad (10)$$

cf. Equation (7). One may expect that the prediction of the local maximum of the vortex soliton at point (10) is valid when it yields values of $(r_{\max}^2)_{\text{TF}}$ which are large enough, i.e., if S and W are relatively large. Indeed, the comparison with the numerically produced profiles of the vortex solitons, displayed below in Figures 6 and 10, demonstrates that Equation (10) predicts, relatively accurately, $(r_{\max})_{\text{TF}} = 4$ for $S = 5$, $W = 2$, $\sigma = -1$, and $g = 0$. However, the prediction given by Equation (10) is not accurate for $S = 1$ and 2.

Finally, in the limit of $r \rightarrow 0$, the asymptotic form of the solution is simple, $u(r, \theta) \approx u_0 r^S$, but constant u_0 cannot be found explicitly, as it depends on the global structure of the vortex soliton solution. In particular, the crude TF approximation given by Equation (9) yields $u_0 = f_0 \left[\alpha + i \left(\frac{2(S+1)}{W^2} + \sigma - g \right) \right]^{-1}$.

2.2. The Variational Approximation (VA)

A consistent global analytical fit for the vortex solitons may be provided by VA based on the Lagrangian of the underlying equation [2]. While Equation (1), which includes the linear dissipative term, does not have a Lagrangian structure, it can be converted into an appropriate form by the substitution, as suggested by Ref. [41], which absorbs the dissipative term:

$$u(r, \theta, t) = U(r, t) e^{iS\theta - \alpha t}, \quad (11)$$

thereby producing the following time-dependent equation for complex function $U(r, t)$, where, as said above, we set $\eta = 1$ by means of scaling:

$$\frac{\partial U}{\partial t} = \frac{i}{2} \left(\frac{\partial^2}{\partial r^2} + \frac{1}{r} \frac{\partial}{\partial r} - \frac{S^2}{r^2} \right) U + i\sigma(|U|^2 e^{-2\alpha t} - 1)U - ig(|U|^4 e^{-4\alpha t} - 1)U + f(r)e^{\alpha t}. \quad (12)$$

The real Lagrangian, which precisely produces the time-dependent Equation (12), is

$$L = \int_0^\infty \left[\frac{i}{2} \left(\frac{\partial U^*}{\partial t} U - U^* \frac{\partial U}{\partial t} \right) + \frac{1}{2} \left| \frac{\partial U}{\partial r} \right|^2 + \left(\frac{S^2}{2r^2} + \sigma - g \right) |U|^2 - \frac{\sigma}{2} e^{-2\alpha t} |U|^4 + \frac{g}{3} e^{-4\alpha t} |U|^6 + i f(r) e^{\alpha t} (U^* - U) \right] r dr. \quad (13)$$

The simplest *ansatz* that may be used as the basis for VA follows the form of the pump term (2):

$$U(r, t) = U_0 e^{i\phi} r^S \exp \left(-\frac{r^2}{W^2} + \alpha t \right), \quad (14)$$

where variational parameters U_0 and ϕ are the real amplitude and phase shift of the solution with respect to the pump. Power (3) for this *ansatz* is

$$P_S = \pi \Gamma(S+1) \left(\frac{W^2}{2} \right)^{S+1} U_0^2, \quad (15)$$

where $\Gamma(S+1) \equiv S!$ is the gamma function, and the time-dependent factors, $\exp(\pm\alpha t)$, mutually cancel when relations (11) and (14) are substituted in expression (3). Note that the local power $|U(r)|^2$, corresponding to *ansatz* (14), attains its maximum at $r^2 = SW^2/2$.

The substitution of *ansatz* (14) in Lagrangian (13) and straightforward integration yields the respective VA Lagrangian:

$$\begin{aligned} L_{VA} = & U_0 e^{2\alpha t} \left\{ \left[6^{-(3S+2)} \Gamma(3S+1) g W^{2(3S+1)} \right] U_0^5 - \left[2^{-4(S+1)} \Gamma(2S+1) \sigma W^{2(2S+1)} \right] U_0^3 \right. \\ & + 2^{-(S+2)} \Gamma(S+1) W^{2S} \left[\left(\frac{d\phi}{dt} + (\sigma - g) \right) W^2 + (S+1) \right] U_0 \\ & \left. + 2^{-(S+1)} \Gamma(S+1) W^{2(S+1)} f_0 \sin \phi \right\}. \end{aligned} \quad (16)$$

Then, the Euler–Lagrange equations for U_0 and ϕ are obtained as

$$\partial L_{VA} / \partial U_0 = \delta L_{VA} / \delta \phi = 0, \quad (17)$$

where $\delta / \delta \phi$ stands for the variational derivative. Taking into regard that Lagrangian (16) must be substituted in the respective action, $\int L_{VA} dt$, and then the action must be actually subjected to the variation, one should apply the time differentiation to factor $e^{2\alpha t}$ in Lagrangian (16) while deducing the appropriate form of $\delta L_{VA} / \delta \phi$ in Equation (17). Once the Euler–Lagrange Equation (17) has been derived, we consider their stationary (fixed-point) solutions by setting $dU_0/dt = d\phi/dt = 0$, which yields

$$U_0 \alpha - f_0 \cos(\phi) = 0, \quad (18)$$

$$\begin{aligned} 6^{-(3S+1)} \Gamma(3S+1) g W^{2(2S+1)} U_0^5 - 2^{-2(2S+1)} \Gamma(2S+1) \sigma W^{2S+2} U_0^3 \\ + 2^{-(S+1)} \Gamma(S+1) \left\{ f_0 W^2 \sin \phi + \left[(\sigma - g) W^2 + (S+1) \right] U_0 \right\} = 0. \end{aligned} \quad (19)$$

It is relevant to mention that the evolution equation for the power (3), which follows from Equation (12), is

$$\frac{dP}{dt} = -2\alpha P + 4\pi \int_0^\infty f(r) \operatorname{Re}\{U(r,t)\} e^{-\alpha t} r dr. \quad (20)$$

The stationary states must satisfy the balance condition, $dP/dt = 0$. Then, the substitution of *ansatz* (14) and expression (2) for the pump in this condition yields a simple relation,

$$\cos \phi = \frac{\alpha U_0}{f_0}, \quad (21)$$

which is identical to Equation (18). In particular, Equation (21) implies that, for the fixed pump's amplitude f_0 , the amplitude of the established localized pattern cannot exceed the maximum value, which corresponds to $\phi = 0$ in Equation (21):

$$U_0 \leq (U_0)_{\max} = f_0 / \alpha. \quad (22)$$

2.3. VA for the Cubic ($g = 0$) and Quintic ($g \rightarrow \infty$) Models

First, we aim to predict stationary states, as solutions of Equations (18) and (19), for the model with cubic-only nonlinearity, i.e., $g = 0$, under the assumption that the loss

and pump terms in Equation (1) may be considered as small perturbations. In the lowest approximation, i.e., dropping the small term $\sim f_0$ in Equation (19), one obtains a relatively simple expression that predicts the squared amplitude of the vortex soliton,

$$(U_0^2)_{\text{VA}}^{(g=0)} = \frac{2^{2S+1}}{(2S-1)!!} W^{-2S} [1 + \sigma(S+1)W^{-2}], \quad (23)$$

with the respective power (15) of the underlying *ansatz* (14) being

$$P_{\text{VA}}^{(g=0)} = \frac{2^S S! \pi}{(2S-1)!!} [W^2 + \sigma(S+1)]. \quad (24)$$

Note that expressions (23) and (24) are always meaningful for the self-focusing sign of the cubic nonlinearity, $\sigma = +1$, while in the case of defocusing, $\sigma = -1$, the expressions are meaningful if they are positive, which imposes a restriction on the width of the Gaussian pump: it must be broad enough, viz.,

$$W^2 > S+1. \quad (25)$$

The dependence of the power given by Equation (24) on the pump's squared width W^2 for three different values of the vorticity, $S = 1, 2, 3$, is plotted in Figure 1a,b for the self-focusing and defocusing signs of the cubic term, i.e., $\sigma = +1$ and -1 , respectively. Note that in Figure 1b for $\sigma = -1$, there is no solution in the region in which condition (25) does not hold, hence, the VA solution does not exist.

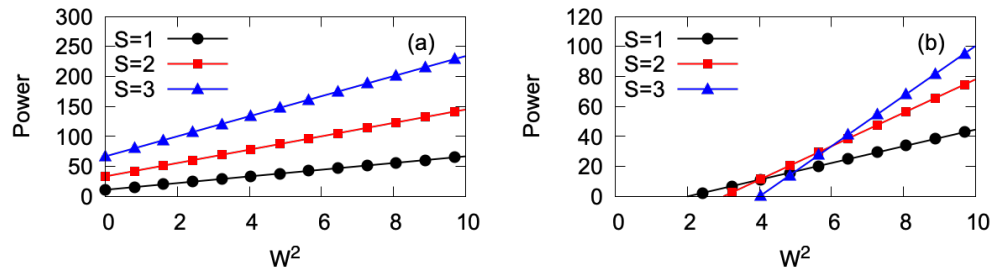


Figure 1. The power of the VA solution, in the case of $g = 0$ (no quintic nonlinearity), vs. the pump's squared width, as given by Equation (24), which neglects weak effects of the pump and loss (small f_0 and α) for the self-focusing ($\sigma = +1$) in (a) and defocusing ($\sigma = -1$) in (b) signs of the cubic term. The black curve with circles, the red one with squares, and the blue one with triangles pertain to vorticities $S = 1, 2$, and 3 , respectively.

In the limit of the dominant quintic nonlinearity, i.e., $g \rightarrow \pm\infty$, opposite to the pure cubic model considered above, the asymptotic solution of Equation (19) is

$$(U_0^2)_{\text{VA}}^{(g \rightarrow \pm\infty)} \approx 2^S \sqrt{3^{3S+1} \frac{S!}{(3S)!}} W^{-2S} \quad (26)$$

(in which the large coefficient g cancels out), with the respective expression for power (15) being

$$P_{\text{VA}}^{(g \rightarrow \pm\infty)} = \frac{3^{(3S+1)/2} \pi (S!)^{3/2}}{2 \sqrt{(3S)!}} W^2, \quad (27)$$

cf. Equations (23) and (24).

In the following section, we report results of the numerical solution of Equation (1) and compare them to solutions of the full system of the VA Equations (18) and (19), which include effects of the pump and loss terms.

3. Numerical Results

Simulations of Equation (1) were conducted by means of the split-step pseudospectral algorithm. The solution procedure started from the zero input and was running until convergence to an apparently stable stationary profile (if this outcome of the evolution was possible). This profile was then compared to its VA counterpart, which was produced by a numerical solution of Equations (18) and (19) with the same values of parameters α , $\sigma = \pm 1$, g , f_0 , W , and S (see Equation (2)). The results are presented below by varying, severally, loss α , vorticity S , the pump's width W , strength f_0 , and, eventually, the quintic coefficient g . The findings were eventually summarized in the form of stability charts plotted in Figure 12.

3.1. Variation in the Loss Parameter α

In Figure 2a, we display the cross-section (drawn through $y = 0$) of the variational and numerical solutions for the stable vortex solitons obtained with $\alpha = 0.5, 1.0$, and 2.0 , while the other parameters were fixed as $\sigma = +1$ (the self-focusing cubic nonlinearity), $g = 0$, $f_0 = 1$, $W = 2$, and $S = 1$. The accuracy of the VA-predicted solutions presented in Figure 2a are characterized by the relative power differences from their numerically found counterparts, which resulted in 5.1%, 3.1%, and 0.5% for

$$\alpha = 0.5, 1.0, 2.0, \quad (28)$$

respectively. Thus, the VA accuracy improves with the increase in α .

Similar results for the self-defocusing nonlinearity, $\sigma = -1$, are presented in Figure 2b, which shows an essentially larger discrepancy between the VA and numerical solutions, *viz.*, 18.9%, 17.4%, and 3.4% for the same set (28) of values of the loss parameter, with the other coefficients being the same as in Figure 2a. The larger discrepancy is explained by the fact that localized (bright soliton) modes are not naturally maintained by the self-defocusing; hence, the ansatz (14), which is natural for the self-trapped solitons in the case of self-focusing, is not accurate enough for $\sigma = -1$. In the same vein, it is natural that, in the latter case, the discrepancy is more salient for stronger nonlinearity, i.e., smaller α , which makes the respective amplitude higher.

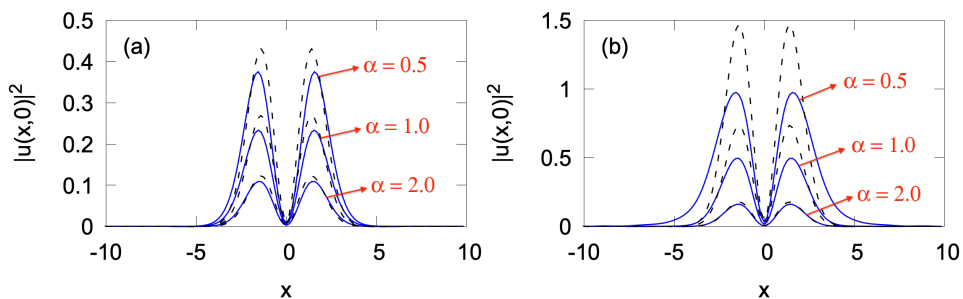


Figure 2. The comparison between cross-sections (drawn through $y = 0$) of the VA solutions and their numerically found counterparts (dashed black and solid blue lines, respectively) for different values of the loss parameter α in Equation (1) taken from set (28). Panels (a,b) pertain to the self-focusing ($\sigma = +1$) and defocusing ($\sigma = -1$) signs of cubic nonlinearity, respectively. The other parameters in Equations (1) and (2) are fixed as $g = 0$, $\eta = 1$, $f_0 = 1$, $W = 2$, and $S = 1$.

There is a critical value of α below which the vortex solitons are unstable. As an example, Figure 3 shows the VA-predicted and numerically produced solutions for $\alpha = 0.2$ and $\sigma = +1$ (self-focusing nonlinearity). The observed picture may be understood as a result of the above-mentioned azimuthal MI, which breaks the axial symmetry of the vortex soliton. More examples of the instability of this type are displayed below. For the values of the other parameters fixed as in Figure 3, the instability boundary was $\alpha_{\text{crit}} \approx 0.35$. The

stabilizing effect of the loss at $\alpha > \alpha_{\text{crit}}$ is a natural feature. On the other hand, the increase in α led to a decrease in the soliton's amplitude, as seen in Figure 2.

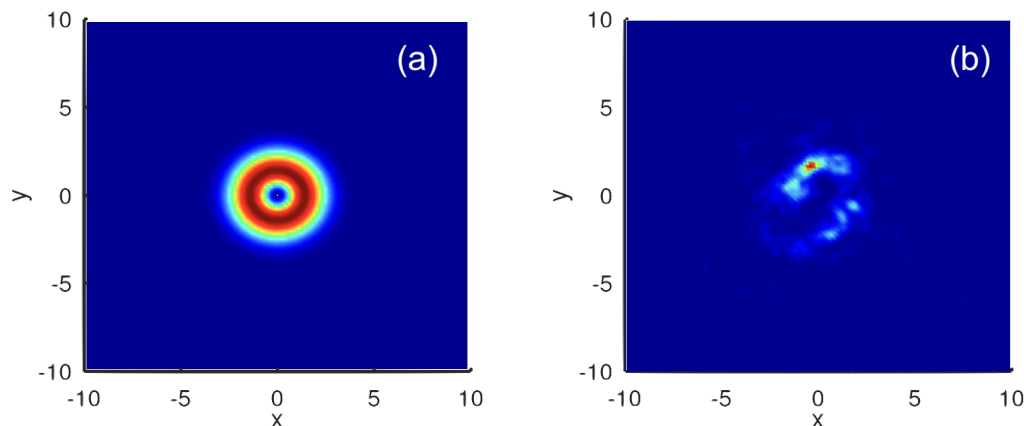


Figure 3. Profiles of $|u|^2$ produced by VA (a) and numerical solution at $t = 100$ (b) in the case of self-focusing ($\sigma = +1$) for $\alpha = 0.2$. Other parameter are the same as in Figure 2a.

In the case of self-defocusing ($\sigma = -1$), all the numerically found vortex modes were stable, at least, at $\alpha \geq 0.1$, although the discrepancy in the values of the power between these solutions and their VA counterparts was very large at small α , thereby exceeding 75% at $\alpha = 0.1$. As mentioned above, the growing discrepancy is explained by the increase in the soliton's amplitude with the decrease in α . At still smaller values of α , the relaxation of the evolving numerical solution toward the stationary state is very slow, which makes it difficult to identify the stability.

3.2. Variation in the Pump's Vorticity S

To analyze the effects of the winding number (vorticity) S , we fixed $g = 0$ (the pure cubic nonlinearity) and set $\alpha = 1$, $f_0 = 1$, $W = 2$ in Equations (1) and (2). In the self-focusing case ($\sigma = +1$), the numerically produced solutions were stable for $S = 1$ and 2 and unstable for $S \geq 3$. In the former case, the power differences between the VA and numerical solutions were 3.1% and 4.9% for $S = 1$ and 2, respectively, i.e., the VA remains a relatively accurate approximation in this case.

In the self-defocusing case ($\sigma = -1$), considering the same values of the other parameters as used above, the numerical solution produced stable vortex solitons at least until $S = 5$. For the same reason as mentioned above, the accuracy of the VA was much lower for $\sigma = -1$ than for the self-focusing case ($\sigma = +1$), with the respective discrepancies in the power values being 17.4%, 6.7%, 24.1%, 29.0%, and 29.6% for $S = 1, 2, 3, 4$, and 5, respectively.

For the cogent verification of the stability of the localized vortices in the case of self-defocusing, we also checked it for smallest value of the loss parameter considered in this work, *viz.*, $\alpha = 0.1$, again for $S = 1, 2, 3, 4$, and 5, and the above-mentioned values of the other coefficients, i.e., $f_0 = 1$ and $W = 2$. Naturally, the discrepancy between the VA and numerical findings was still higher in this case, being 75%, 72.5%, 65.7%, 55.2%, and 41.1% for $S = 1, 2, 3, 4$, and 5, respectively. The result is illustrated in Figure 4 for a relatively large vorticity, $S = 4$. In particular, the pattern of $|u(x, y)|^2$ and the corresponding cross-section, displayed in Figure 4b,c, respectively, exhibit the established vortex structure and background “garbage” produced by the evolution.

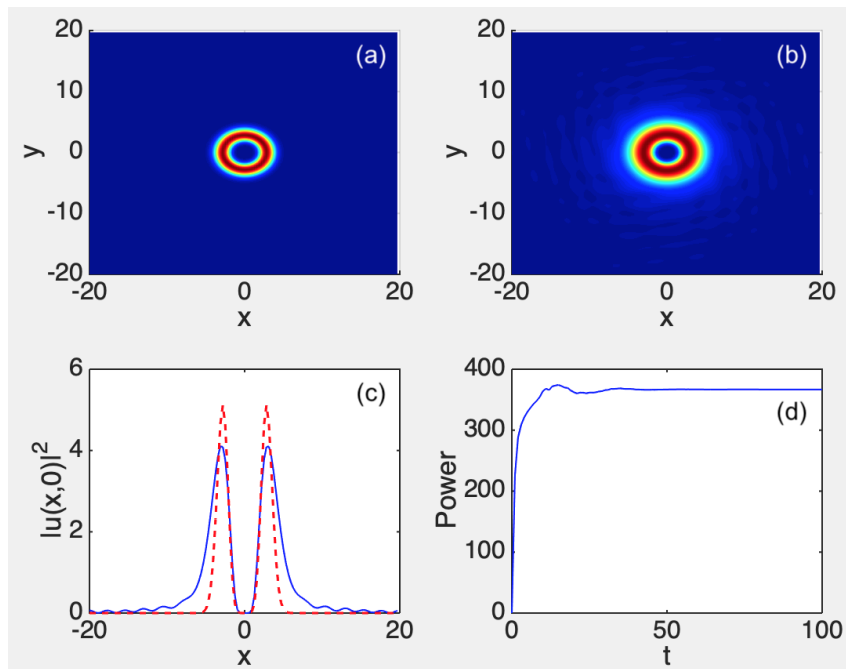


Figure 4. (a) The VA-predicted pattern and (b) the corresponding result of the direct simulation of Equation (1) with $\sigma = -1$ and $g = 0$ (cubic self-defocusing) at $t = 100$, initiated by the zero input at $t = 0$ for $\alpha = 0.1$, $f_0 = 1$, $W = 2$, and vorticity $S = 4$ in the pump term (2). (c) The respective cross-sections drawn through $y = 0$. (d) The evolution of the total power P (see Equation (3) of the numerical solution in the course of the simulation.

3.3. Variation in the Pump's Width W

To address the effects of the variation in parameter W in Equation (2), we fixed $g = 0$, $\alpha = 1$, $f_0 = 1$, and $S = 1$. In Figure 5a, the power of the VA-predicted and numerically found stable vortex soliton solutions are plotted as a function of W for both the self-focusing and defocusing cases, i.e., $\sigma = +1$ and $\sigma = -1$, respectively. In the former case, the azimuthal MI set in at $W \geq 2.7$; see an example in Figure 5b for $W = 2.75$.

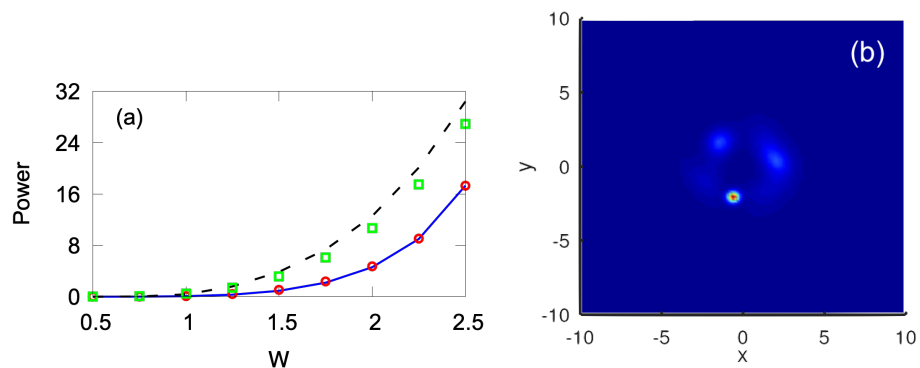


Figure 5. (a) The power of the VA-predicted vortex soliton solutions (solid blue and dashed black lines pertaining to the self-focusing, $\sigma = +1$, and self-defocusing, $\sigma = -1$, cubic nonlinearity, respectively) and their numerically found counterparts (red circles and green squares pertaining to the self-focusing and self-defocusing nonlinearity, respectively) vs. the pump's width W . Other parameters are $g = 0$, $\alpha = 1$, $f_0 = 1$, and $S = 1$. (b) The profile produced, at $t = 100$, by the numerically generated unstable solution in the case of the self-focusing, $\sigma = +1$, with $W = 2.75$.

In the self-focusing case, $\sigma = +1$, the azimuthal MI for the solitons with higher vorticities, $S = 2, 3, 4$, or 5 , set in at $W \geq 2.1, 1.7, 1.6$, and 1.4 , respectively. In the self-defocusing case, no existence/stability boundary was found for the vortex modes with

$S = 1$, $S = 2$, and $S = 3$ (at least up to $W = 5$). At higher values of the vorticity, the localized vortices do not exist; in the defocusing case, they exist at $W > 3.5$ and $W > 2.5$ for $S = 4$ and $S = 5$, respectively.

3.4. Variation in the Pump's Strength f_0

The effects of the variation in f_0 are reported here, where we fixed the other parameters as $g = 0$, $\alpha = 1$, and $W = 2$. In the case of the cubic self-focusing, $\sigma = +1$, the vortex soliton with $S = 1$ was subject to an MI at $f_0 \geq 1.6$. As a typical example, in Figure 6, we display the VA-predicted solution alongside the result of the numerical simulations for $f_0 = 1.7$. For higher vorticities, $S = 2, 3, 4$, and 5 , the azimuthal instability set in at $f_0 \geq 1.1, 0.6, 0.3$, and 0.08 , respectively. Naturally, the narrow vortex rings with large values of S are much more vulnerable to the quasi-one-dimensional azimuthal MI.

The power of the vortex solitons with $S = 1$ and 2 , as produced by the VA and numerical solution, is plotted vs. the pump amplitude f_0 in Figure 7a. As an example, Figure 7b showcases an example of the cross-section profile of the vortex soliton with $S = 2$, thus demonstrating the reliability of the VA prediction. In the range of $f_0 \leq 1$, the highest relative difference in the power between the numerical and variational solutions cases was 5.5% and 7.5% for $S = 1$ and $S = 2$, respectively.

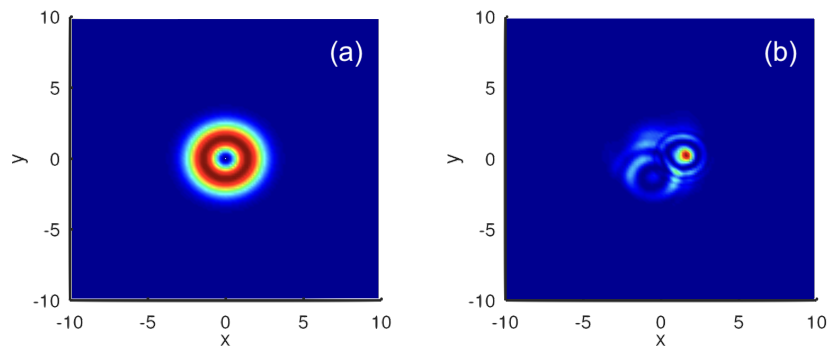


Figure 6. (a) The VA-predicted profile of $|u|^2$ in the self-focusing case, with parameters $g = 0$, $\sigma = +1$, $\alpha = 1$, $f_0 = 1.7$, $W = 2$, and $S = 1$. (b) The unstable solution, produced at $t = 100$, by the simulations of Equation (1) for the same parameters.

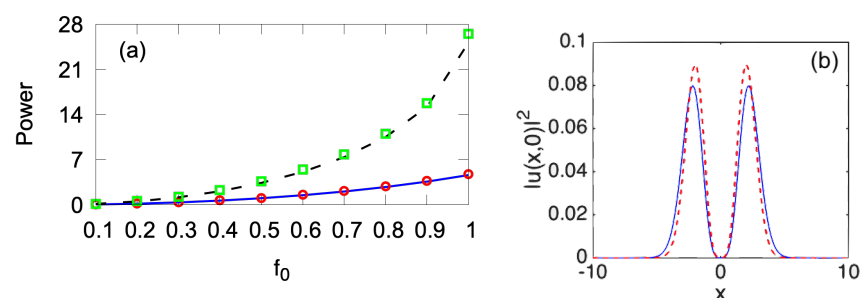


Figure 7. (a) The power versus f_0 for the confined vortex modes in the self-focusing case ($\sigma = +1$). The VA solutions for $S = 1$ and 2 are shown by solid blue and dashed black lines, respectively. The corresponding numerical solutions are represented by red circles and green squares, respectively. Recall that the numerical solutions are stable, in this case, at $f_0 < 1.6$ and $f_0 < 1.1$ for $S = 1$ and 2 , respectively. (b) The VA-predicted and numerically obtained (the dashed red and solid blue lines, respectively) profiles of the stable solution with $S = 2$ and $f_0 = 0.4$, drawn as cross-sections through $y = 0$. The other parameters are $g = 0$, $\sigma = +1$, $\alpha = 1$, $W = 2$.

It is relevant to mention that the “traditional” azimuthal instability of vortex ring solitons with a winding number S demonstrates the fission of the original axially symmetric shape into a set consisting of a large number $N \geq S$ of symmetrically placed localized

fragments [2,40], while the above examples, displayed in Figures 3b, 5b, and 6b, demonstrate the appearance of a single bright fragment and a “garbage cloud” distributed along the original ring. At larger values of f_0 , our simulations produced examples of the “clean” fragmentation, *viz.*, with $N = 4$ produced by the unstable vortex rings with $S = 1$ in Figure 8a, $N = 5$ produced by $S = 2$ and 3 in Figure 8b,d, $N = 7$ by $S = 2$ and 3 in Figure 8c,e, and $N = 8$ by $S = 3$ in Figure 8f. These outcomes of the instability development were observed at the same evolution time of $t = 100$ as in Figures 3b, 5b, and 6b. The gradual increase in the number of the fragments on S is explained by the dependence of the azimuthal index of the fastest growing eigenmode of the breaking instability on the underlying winding number S , which is a generic property of vortex solitons [2,40].

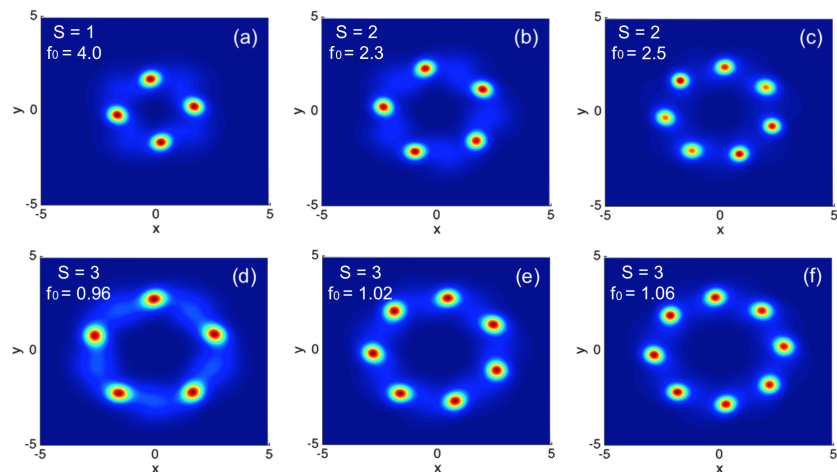


Figure 8. Examples of the fission of unstable vortex ring solitons produced by simulations of the LL Equation (1), with $\sigma = +1$ (cubic self-focusing), $g = 0$ (no quintic nonlinearity), $\alpha = 2$, $W = 2$, and $\eta = 1$. Each plot displays the result of the numerical simulations at time $t = 100$. Values of the initial vorticity and pump’s strength are indicated in panels.

In the self-defocusing case, $\sigma = -1$, a summary of the results produced by the VA and numerical solution for the stable vortex solitons with $S = 1$ and 2, in the form of the dependence of their power on f_0 , is produced in Figure 9a (cf. Figure 7a for $\sigma = +1$). Naturally, the VA–numerical discrepancy increases with the growth of the pump’s strength, f_0 ; see an example in Figure 9b. Unlike the case of $\sigma = +1$, in the case of self-defocusing the vortex modes with $S \leq 5$ remained stable, at least, up to $f_0 = 5$ (here, we do not consider the case of $S > 5$).

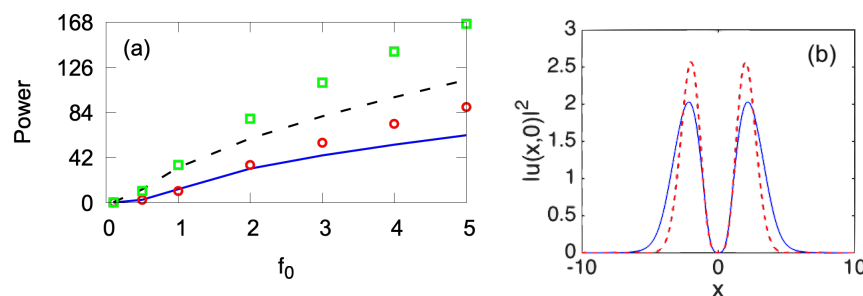


Figure 9. (a) The power versus f_0 for the vortex modes in the self-defocusing case ($\sigma = -1$). The VA solutions for $S = 1$ and 2 are shown by solid blue and dashed black lines, respectively. The corresponding numerical solutions are presented by red circles and green squares, respectively. (b) The VA-predicted and numerically obtained (the dashed red and solid blue lines, respectively) profiles of the solution with $S = 2$ and $f_0 = 2$ drawn as the cross-sections through $y = 0$. The other parameters are $g = 0$, $\sigma = -1$, $\alpha = 1$, $W = 2$.

3.5. Influence of the Quintic Coefficient g

In the above analysis, the quintic term was dropped in the LL Equation (1), thus setting $g = 0$. To examine the impact of this term, we first addressed the case shown above in Figure 3, which demonstrated that the vortex soliton with $S = 1$, as a solution to Equations (1) and (2) with $g = 0$, $\sigma = +1$ and $f_0 = 1$, $W = 2$, was unstable if the loss parameter fell below the critical value of $\alpha = 0.35$. We found that adding to Equation (1) the quintic term with either $g = -1$ or $g = +1$ (the self-focusing or defocusing quintic nonlinearity, respectively) led to the *stabilization* of the vortex mode displayed in Figure 3, which was unstable in the absence of the quintic term. The stabilization of the soliton by quintic self-defocusing is a natural fact. More surprising is the possibility to provide the stabilization by self-focusing quintic nonlinearity because, in most cases, the inclusion of such a term gives rise to the supercritical collapse in 2D, thus making all solitons strongly unstable [2,40]. However, it is concluded from the stability charts displayed below in Figure 12 that the stabilizing effect of the quintic self-focusing occurs only at moderately small powers, for which the quintic term was not a clearly dominant one. In the general case, the soliton stability regions naturally shrunk in Figure 12 under the action of the quintic self-focusing quintic term, with $g < 0$.

In the presence of the quintic term, the comparison of the numerically found stabilized vortex soliton profiles with their VA counterparts, whose parameters were produced by a numerical solution of Equations (18) and (19), is presented in Figure 10. Similar to the results for the LL equation with the cubic-only nonlinearity, the VA is essentially more accurate in the case of the self-focusing sign of the quintic term ($g < 0$) than in the opposite case, where $g > 0$. In particular, in the case shown in Figure 10, the power-measured discrepancy for $g = -1$ and $+1$ was, respectively, 4% and 64%. An explanation for this observation is provided by the fact that the soliton's amplitude was much higher in the latter case.

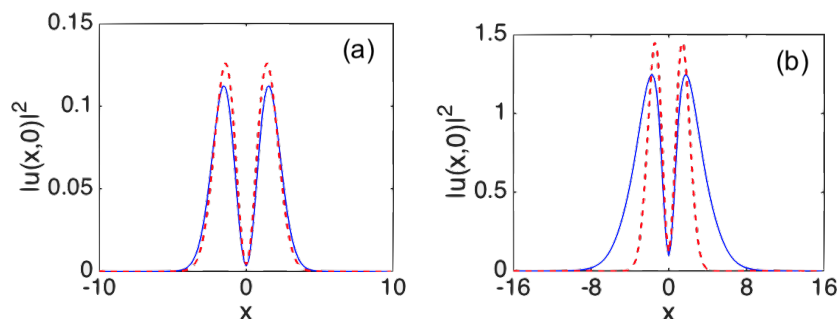


Figure 10. Cross-section profiles (drawn through $y = 0$) for stable vortex solitons with $S = 1$, produced by Equation (1) with the quintic self-focusing $g = -1$ (a) or defocusing $g = +1$ (b) term. In both cases, the cubic self-focusing cubic term, with $\sigma = +1$, is present. The numerically found profiles and their VA-produced counterparts are displayed, respectively, by the solid blue and dashed lines. Other parameters are $\alpha = 0.2$, $\eta = 1$, and $f_0 = 1$, $W = 2$.

Another noteworthy finding is the stabilization of higher-vorticity solitons by the quintic term. For instance, it was shown above that, for parameters $\alpha = 1$, $\eta = 1$, $f_0 = 1$, $W = 2$, $g = 0$, and $\sigma = +1$ (the cubic self-focusing), all vortex solitons with $S \geq 3$, produced by Equation (1), were unstable. Now, we demonstrate that the soliton with $S = 3$ is stabilized by adding the self-defocusing quintic term with a small coefficient, just $g = 0.1$; see Figure 11b. As a counterintuitive effect, the stabilization of the same soliton by the self-focusing quintic term was possible too, but the necessary coefficient was large, $g = -6$; see Figure 11a (recall that $g = -1$ is sufficient for the stabilization of the vortex soliton with $S = 1$ and $\alpha = 0.2$ in Figure 10a). Nevertheless, similar to what has been said above, the set of Figure 12c,f,i demonstrates the natural shrinkage of the stability area under the action of quintic self-focusing. For the stabilized vortex modes shown in Figure 11a—in the case when both the cubic and quintic terms are self-focusing—the relative power-measured

discrepancy between the numerical and VA-predicted solutions was very small, $\approx 0.7\%$, while in the presence of the weak quintic self-defocusing in Figure 11b, the discrepancy was 6.6%.

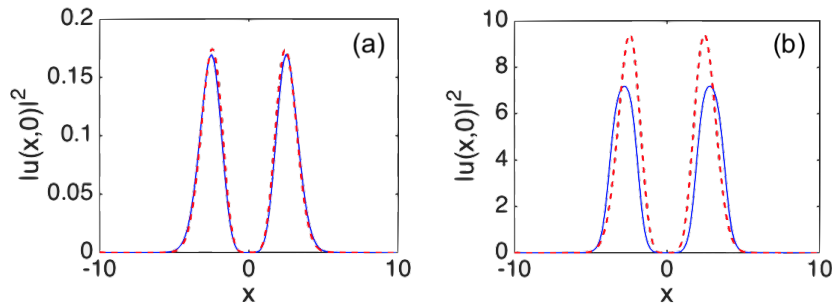


Figure 11. Cross-section profiles (drawn through $y = 0$) of vortex solitons with $S = 3$, stabilized by the self-focusing (a) or defocusing (b) quintic term in Equation (1), with the respective coefficient $g = -6$ or $g = 0.1$, with other parameters being $\sigma = -1$ (cubic self-focusing), $\alpha = 1$, $\eta = 1$, and $f_0 = 1$, $W = 2$ in Equation (2). The numerically found solutions and their VA-predicted counterparts are plotted by the solid blue and dashed red lines, respectively.

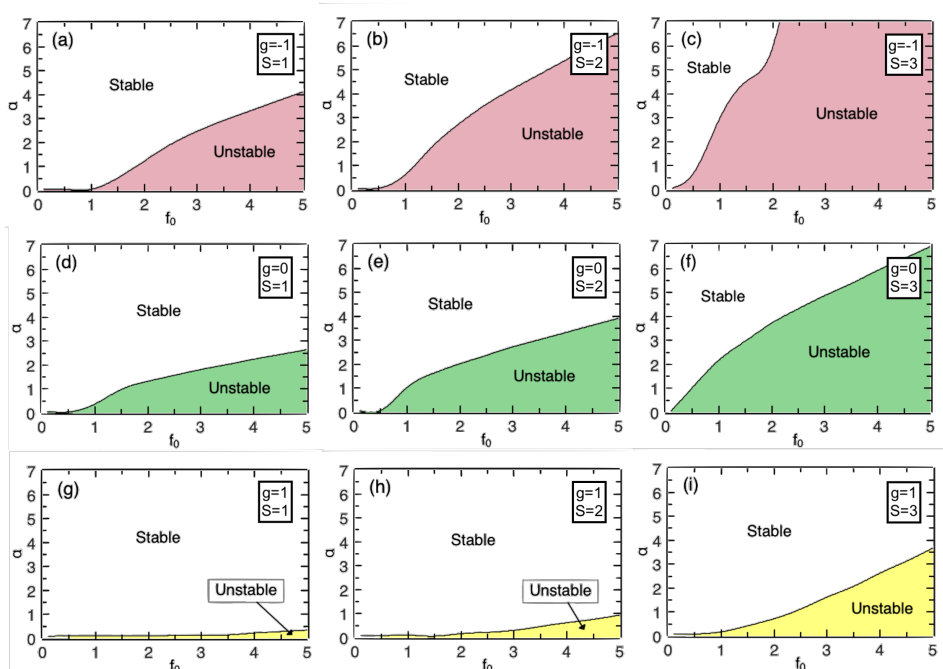


Figure 12. Stability areas for families of the vortex solitons with winding numbers $S = 1, 2$, and 3 , in the plain of the loss coefficient (α) and amplitude of the pump beam (f_0), for three different values of the quintic coefficient, $g = -1, 0, +1$ (recall that $g < 0$ and $g > 0$ correspond, respectively, to the self-focusing and defocusing). Other parameters of Equations (1) and (2) are $\sigma = +1$ (the self-focusing cubic term), $\eta = 1$, and $W = 2$.

3.6. Stability Charts in the Parameter Space

The numerical results produced in this work are summarized in the form of stability areas plotted in Figure 12 in the parameter plane (f_0, α) , for the vortex soliton families with winding numbers $S = 1, 2, 3$, and three values of the quintic coefficient, $g = -1, 0, +1$, while the cubic term is self-focusing, $\sigma = +1$, and the width of the pump beam is fixed, $W = 2$. In addition to that, stability charts corresponding to the combination of the cubic self-defocusing ($\sigma = -1$) and quintic focusing ($g = -1$), also for $S = 1, 2, 3$, are plotted in Figure 13.

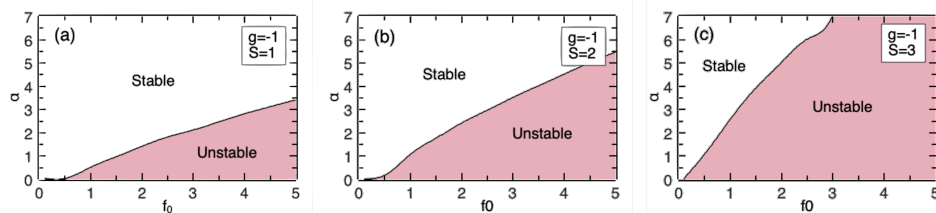


Figure 13. The same as in Figure 12a–c but for $\sigma = -1$ and $g = -1$ (the cubic self-defocusing and quintic focusing terms).

The choice of the parameter plane (f_0, α) in the stability diagrams displayed in Figure 12 is relevant, as the strength of the pump beam, f_0 , and loss coefficient, α , are amenable to accurate adjustment in the experiment (in particular, α may be tuned by partially compensating the background loss of the optical cavity by a spatially uniform pump taken separately from the confined pump beam). As seen in all panels of Figures 12 and 13, the increase in α naturally provides effective stabilization of the vortex modes, while none of them are stable at $\alpha = 0$, which is in agreement with the known properties of vortex soliton solutions of the 2D nonlinear Schrödinger equation with the cubic and/or cubic–quintic nonlinearity [2,40]. The apparent destabilization of the vortices with the increase in the pump’s amplitude f_0 is explained by the ensuing enhancement of the destabilizing nonlinearity. Other natural features exhibited by Figure 12 are the general stabilizing/destabilizing effect of the quintic self-defocusing/focusing (as discussed above) and expansion of the splitting instability area with the increase in S (the latter feature is also exhibited by Figure 13). The latter finding is natural too, as a larger S makes the ring-shaped mode closer to the quasi-1D shape (see, in particular, Figure 8), which facilitates the onset of the above-mentioned azimuthal MI (modulational instability).

Thus, the inference is that the instability mode, which determines the boundary of the stability areas, in Figures 12 and 13 is the breaking of the axial symmetry of the vortex rings by azimuthal perturbations, as shown above, in particular, in Figures 3b, 5b, and 6b. The destabilization through the spontaneous splitting of the rings into symmetric sets of fragments (see Figure 8) occurs deeply inside the instability area, i.e., at larger values of f_0 .

4. Conclusions

We have introduced the two-dimensional LL (Lugiato–Lefever) equation including the self-focusing or defocusing cubic or cubic–quintic nonlinearity and the confined pump with embedded vorticity (winding number), $S \leq 5$. Stable states in the form of vortex solitons (rings) for these values of S were obtained, in parallel, in the semianalytical form by means of VA (variational approximation) and numerically, by means of systematic simulations of the LL equation starting from the zero input. The VA provided much more accurate results in the case of the self-focusing nonlinearity than for the defocusing system. Stability areas of the vortex solitons with $S = 1, 2, 3$ were identified in the plane of experimentally relevant parameters, *viz.*, the pump amplitude and loss coefficient, for the self-focusing and defocusing signs of the cubic and quintic terms. Stability boundaries for the vortex rings were determined by the onset of the azimuthal instability, which broke their axial symmetry. These findings suggest new possibilities for the design of tightly confined robust optical modes, such as vortex pixels.

As an extension of this work, it may be interesting to construct solutions pinned to a symmetric pair of pump beams with or without intrinsic vorticity. In this context, it is possible to consider the beam pair with identical or opposite vorticities. In the case of the self-focusing sign of nonlinearity, one may expect an onset of spontaneous breaking of the symmetry in the dual-pump configuration. Results for this setup will be reported elsewhere.

Author Contributions: S.K.: Investigation, Formal analysis, Numerical Simulations, Validation, Visualization, Writing—original draft; W.B.C.: Conceptualization, Methodology, Formal analysis, Investigation, Numerical Simulations, Validation, Writing—review and editing; B.A.M.: Supervision, Conceptualization, Methodology, Formal analysis, Project administration, Data curation, Validation, Writing—review and editing. All authors have read and agreed to the published version of the manuscript.

Funding: The work of S.K. and B.A.M. is supported, in part, by the Israel Science Foundation through grant No. 1695/22. W.B.C. acknowledges the financial support of the Brazilian agency CNPq (grant #306105/2022-5). This work was also performed as a part of program #465469/2014-0 of the Brazilian National Institute of Science and Technology (INCT) for Quantum Information.

Data Availability Statement: Detailed data may be provided upon a reasonable request

Acknowledgments: We thank Branko Dragovich for invitation to submit the paper to the Special Issue of Symmetry on the topic of “Selected Papers on Nonlinear Dynamics”.

Conflicts of Interest: The authors declare no conflicts of interest.

References

1. Kivshar, Y.S.; Agrawal, G. *Optical Solitons: From Fibers to Photonic Crystals*; Elsevier Science: Amsterdam, The Netherlands, 2003. [[CrossRef](#)]
2. Malomed, B.A. *Multidimensional Solitons*; American Institute of Physics Publishing: Melville, NY, USA, 2022.
3. Rosanov, N.N. *Spatial Hysteresis and Optical Patterns*; Springer: Berlin, Germany, 2002.
4. Ferreira, M.F.S. (Ed.) *Dissipative Optical Solitons*; Springer Nature Switzerland AG: Cham, Switzerland, 2022.
5. Grelu, P.; Akhmediev, N. Dissipative solitons for mode-locked lasers. *Nat. Phot.* **2012**, *6*, 84–92. [[CrossRef](#)]
6. Jiang, M.X.; Wang, X.N.; Ouyang, Q.; Zhang, H. Spatiotemporal chaos control with a target wave in the complex Ginzburg-Landau equation system. *Phys. Rev. E* **2004**, *69*, 56202. [[CrossRef](#)] [[PubMed](#)]
7. Lugiato, L.A.; Lefever, R. Spatial Dissipative Structures in Passive Optical Systems. *Phys. Rev. Lett.* **1987**, *58*, 2209. [[CrossRef](#)] [[PubMed](#)]
8. Tlidi, M.; Panajotov, K. Two-dimensional dissipative rogue waves due to time-delayed feedback in cavity nonlinear optics. *Chaos* **2017**, *27*, 013119. [[CrossRef](#)] [[PubMed](#)]
9. Panajotov, K.; Clerc, M.G.; Tlidi, M. Spatiotemporal chaos and two-dimensional dissipative rogue waves in Lugiato-Lefever model. *Eur. Phys. J. D* **2017**, *71*, 176. [[CrossRef](#)]
10. Tlidi, M.; Taki, M. Rogue waves in nonlinear optics. *Adv. Opt. Photonics* **2022**, *14*, 87–147. [[CrossRef](#)]
11. Sun, Y.; Parra-Rivas, P.; Mangini, F.; Wabnitz, S. Multidimensional localized states in externally driven Kerr cavities with a parabolic spatiotemporal potential: A dimensional connection. *arXiv* **2024**, arXiv:2401.15689.
12. de Valcárcel, G.J.; Staliunas, K. Phase-bistable Kerr cavity solitons and patterns. *Phys. Rev. A* **2013**, *87*, 043802. *PhysRevA.87.043802*. [[CrossRef](#)]
13. Coen, S.; Randle, H.G.; Sylvestre, T.; Erkintalo, M. Modeling of octave-spanning Kerr frequency combs using a generalized mean-field Lugiato-Lefever model. *Opt. Lett.* **2013**, *38*, 37–39. [[CrossRef](#)]
14. Lamont, M.R.E.; Okawachi, Y.; Gaeta, A.L. Route to stabilized ultrabroadband microresonator-based frequency combs. *Opt. Lett.* **2013**, *38*, 3478–3481. [[CrossRef](#)]
15. Godey, C.; Balakireva, I.V.; Coillet, A.; Chembo, Y.K. Stability analysis of the spatiotemporal Lugiato-Lefever model for Kerr optical frequency combs in the anomalous and normal dispersion regimes. *Phys. Rev. A* **2014**, *89*, 063814. [[CrossRef](#)]
16. Lobanov, V.E.; Lihachev, G.; Kippenberg, T.J.; Gorodetsky, M.L. Frequency combs and platicons in optical microresonators with normal GVD. *Opt. Exp.* **2015**, *23*, 7713–7721. [[CrossRef](#)] [[PubMed](#)]
17. Karpov, M.; Guo, H.; Kordts, A.; Brasch, V.; Pfeiffer, M.H.; Zervas, M.; Geiselmann, M.; Kippenberg, T.J. Raman Self-Frequency Shift of Dissipative Kerr Solitons in an Optical Microresonator. *Phys. Rev. Lett.* **2016**, *116*, 103902. [[CrossRef](#)] [[PubMed](#)]
18. Copie, F.; Conforti, M.; Kudlinski, A.; Mussot, A.; Trillo, S. Competing Turing and Faraday Instabilities in longitudinally modulated passive resonators. *Phys. Rev. Lett.* **2016**, *116*, 143901. [[CrossRef](#)] [[PubMed](#)]
19. Parra-Rivas, P.; Gomila, D.; Colet, P.; Gelens, L. Interaction of solitons and the formation of bound states in the generalized Lugiato-Lefever equation. *Eur. Phys. J. D* **2017**, *71*, 198. [[CrossRef](#)]
20. Clerc Gavilán, M.; Ferre, M.A.; Coulibaly, S.; Rojas, R.G.; Tlidi, M. Chimera-like states in an array of coupled-waveguide resonators. *Opt. Lett.* **2017**, *42*, 2906–2909. [[CrossRef](#)] [[PubMed](#)]
21. Garbin, B.; Wang, Y.; Murdoch, S.G.; Oppo, G.-L.; Coen, S.; Erkintalo, M. Experimental and numerical investigations of switching wave dynamics in a normally dispersive fibre ring resonator. *Eur. Phys. J. D* **2017**, *71*, 240. [[CrossRef](#)]
22. Li, Q.; Briles, T.C.; Westly, D.A.; Drake, T.E.; Stone, J.R.; Illic, B.R.; Diddams, S.A.; Papp, S.B.; Srinivasan, K. Stably accessing octave-spanning microresonator frequency combs in the soliton regime. *Optica* **2017**, *4*, 193–203. [[CrossRef](#)] [[PubMed](#)]
23. Lugiato, L.A.; Prati, F.; Gorodetsky, M.L.; Kippenberg, T. From the Lugiato-Lefever equation to microresonator-based soliton Kerr frequency combs. *Phil. Trans. R. Soc. A* **2018**, *376*, 20180113. [[CrossRef](#)]

24. Dong, X.; Spiess, C.; Bucklew, V.G.; Renninger, W.H. Chirped-pulsed Kerr solitons in the Lugiato-Lefever equation with spectral filtering. *Phys. Rev. Res.* **2021**, *3*, 033252. [[CrossRef](#)]
25. Huang, S.-W.; Yang, J.; Yang, S.-H.; Yu, M.; Kwong, D.-L.; Zelevinsky, T.; Jarrahi, M.; Wong, C.W. Globally stable microresonator Turing pattern formation for coherent high-power THz radiation on-chip. *Phys. Rev. X* **2017**, *7*, 041002. [[CrossRef](#)]
26. Kartashov, Y.V.; Alexander, O.; Skryabin, D.V. Multistability and coexisting soliton combs in ring resonators: The Lugiato-Lefever approach. *Opt. Express* **2017**, *25*, 11550–11555. [[CrossRef](#)] [[PubMed](#)]
27. Coillet, A.; Balakireva, I.; Henriet, R.; Saleh, K.; Larger, L.; Dudley, J.M.; Menyuk, C.R.; Chembo, Y.K. Azimuthal Turing patterns, bright and dark cavity solitons in Kerr combs generated with whispering-gallery-mode resonators. *IEEE Photonics J.* **2013**, *5*, 6100409. [[CrossRef](#)]
28. Chembo, Y.K.; Menyuk, C.R. Spatiotemporal Lugiato-Lefever formalism for Kerr-comb generation in whispering-gallery-mode resonators. *Phys. Rev. A* **2013**, *87*, 053852. [[CrossRef](#)]
29. Taheri, H.; Eftekhar, A.A.; Wiesenfeld, K.; Adibi, A. Soliton Formation in Whispering-Gallery-Mode Resonators via Input Phase Modulation. *IEEE Photonics J.* **2015**, *7*, 2200309. [[CrossRef](#)]
30. Wang, Y.-Y.; Li, M.-M.; Zhou, G.-Q.; Fan, Y.; Lai, X.-J. Rotating vortex-like soliton in a whispering gallery mode microresonator. *Eur. Phys. J. Plus* **2019**, *134*, 161. [[CrossRef](#)]
31. Daugey, T.; Billet, C.; Dudley, J.; Merolla, J.-M.; Chembo, Y.K. Kerr optical frequency comb generation using whispering-gallery-mode resonators in the pulsed-pump regime. *Phys. Rev. A* **2021**, *103*, 023521. [[CrossRef](#)]
32. Cao, Q.-H.; Geng, K.-L.; Zhu, B.-W.; Wang, Y.-Y.; Dai, C.-Q. Scalar vortex solitons and vector dipole solitons in whispering gallery mode optical microresonators. *Chaos Sol. Fract.* **2023**, *166*, 112895. [[CrossRef](#)]
33. Cardoso, W.B.; Salasnich, L.; Malomed, B.A. Localized solutions of Lugiato-Lefever equations with focused pump. *Sci. Rep.* **2017**, *7*, 16876. [[CrossRef](#)]
34. Cardoso, W.B.; Salasnich, L.; Malomed, B.A. Zero-dimensional limit of the two-dimensional Lugiato-Lefever equation. *Eur. Phys. J. D* **2017**, *71*, 112. [[CrossRef](#)]
35. Quiroga-Teixeiro, M.; Michinel, H. Stable azimuthal stationary state in quintic nonlinear optical media. *J. Opt. Soc. Am. B* **1997**, *14*, 2004–2009. [[CrossRef](#)]
36. Boudebs, G.; Cherukulappurath, S.; Leblond, H.; Troles, J.; Smekta, F.; Sanchez, F. Experimental and theoretical study of higher-order nonlinearities in chalcogenide glasses. *Opt. Commun.* **2003**, *219*, 427–432. [[CrossRef](#)]
37. Reyna, A.S.; de Araújo, C.B. High-order optical nonlinearities in plasmonic nanocomposites—A review. *Adv. Opt. Photonics* **2017**, *9*, 720–774. [[CrossRef](#)]
38. Andrews, D.L. symmetry and quantum features in optical vortices. *Symmetry* **2021**, *13*, 1368. [[CrossRef](#)]
39. Ramanik, A.; Hung, N.V.; Giersig, M.; Kempa, K.; Konotop, V.V.; Trippenbach, M. Vortex creation without stirring in coupled ring resonators with gain and loss. *Symmetry* **2018**, *10*, 195. [[CrossRef](#)]
40. Malomed, B.A. (INVITED) Vortex solitons: Old results and new perspectives. *Phys. D* **2019**, *399*, 108–137. [[CrossRef](#)]
41. Bullough, R.K.; Fordy, A.P.; Manakov, S.V. Adiabatic invariants theory of near-integrable systems with damping. *Phys. Lett. A* **1982**, *91*, 98–100. [[CrossRef](#)]

Disclaimer/Publisher’s Note: The statements, opinions and data contained in all publications are solely those of the individual author(s) and contributor(s) and not of MDPI and/or the editor(s). MDPI and/or the editor(s) disclaim responsibility for any injury to people or property resulting from any ideas, methods, instructions or products referred to in the content.